

## ADAS analysis of the differential emission measure structure of the inner solar corona

### II. A study of the “quiet Sun” inhomogeneities from SOHO CDS-NIS spectra<sup>\*</sup>

A. C. Lanzafame<sup>1</sup>, D. H. Brooks<sup>2</sup>, and J. Lang<sup>3</sup>

<sup>1</sup> Dipartimento di Fisica e Astronomia, Università di Catania, via S. Sofia 78, 95123 Catania, Italy  
e-mail: alanzafame@ct.astro.it

<sup>2</sup> Kwasan Observatory, Kyoto University, Yamashina, Kyoto 607-8471, Japan

<sup>3</sup> Rutherford Appleton Laboratory, Chilton, Didcot, OX11 0QX, UK

Received 4 October 2004 / Accepted 20 November 2004

**Abstract.** We present a study of the differential emission measure (DEM) of a “quiet Sun” area observed in the extreme ultraviolet at normal incidence by the Coronal Diagnostic Spectrometer (CDS) on the SOHO spacecraft. The data used for this work were taken using the NISAT\_S observing sequence. This takes the full wavelength ranges from both the NIS channels (308–381 Å and 513–633 Å) with the 2 arcsec by 240 arcsec slit, which is the narrowest slit available, yielding the best spectral resolution. In this work we contrast the DEM from subregions of  $2 \times 80$  arcsec<sup>2</sup> with that obtained from the mean spectrum of the whole raster ( $20 \times 240$  arcsec<sup>2</sup>). We find that the DEM maintains essentially the same shape in the subregions, differing by a constant factor between 0.5 and 2 from the mean DEM, except in areas where the electron density is below  $2 \times 10^7$  cm<sup>-3</sup> and downflow velocities of 50 km s<sup>-1</sup> are found in the transition region. Such areas are likely to contain plasma departing from ionisation equilibrium, violating the basic assumptions underlying the DEM method. The comparison between lines of Li-like and Be-like ions may provide further evidence of departure from ionisation equilibrium. We find also that line intensities tend to be lower where velocities of the order of 30 km s<sup>-1</sup> or higher are measured in transition region lines. The DEM analysis is also exploited to improve the line identification performed by Brooks et al. (1999) and to investigate possible elemental abundance variations from region to region. We find that the plasma has composition close to photospheric in all the subregions examined.

**Key words.** Sun: atmosphere – Sun: corona – Sun: UV radiation – Sun: abundances – atomic data – techniques: spectroscopic

### 1. Introduction

The discovery of highly dynamical phenomena in the “quiet Sun” (QS), like blinkers (Harrison 1997; Harrison et al. 1999) or explosive events (Innes et al. 1997), place further questions on the validity of analysis methods which, like the DEM, rely on plasma equilibrium. Indeed, many other small-scale transient phenomena have been reported in the literature, including an attempt to obtain a global view of such processes (Harrison et al. 2003) and for all such events care should be taken to check the validity of the analysis method, particularly whenever a DEM is invoked. The controversy on the validity of analysis methods based on emission measure is rooted, in fact, both on the ill-posed nature of the mathematical problem and on the assumption of ionisation equilibrium, which can be violated by the evolution of the plasma on time-scales comparable to

the ionisation/recombination time-scales. In addition to these concerns, the DEM can be rendered unreliable due to injudicious selection of emission lines, for example, those affected by opacity, or those for which the atomic coefficients are less accurate or incorrectly modelled.

It is crucial, therefore, to understand *where* and *when* emission measure type analyses can give reliable results. Answering such questions has important consequences for establishing the reliability of the physical quantities and the atmospheric morphology extracted from observational data.

Lanzafame et al. (2002), hereafter Paper I, have studied the validity and limitations of the DEM method in abundance determination, spectral line identification, intensity predictions, and validation of atomic cross-sections by analysing the SERTS-89 active region (AR) spectrum (Thomas & Neupert 1994). The integral inversion to infer the DEM distribution from spectral line intensities was performed by the *data adaptive smoothing approach* (Thompson 1990, 1991), using an analysis procedure integrated in ADAS (the Atomic Data and

<sup>\*</sup> Table 5 is only available in electronic form at the CDS via anonymous ftp to cdsarc.u-strasbg.fr (130.79.128.5) or via <http://cdsweb.u-strasbg.fr/cgi-bin/qcat?J/A+A/432/1063>

Analysis Structure). ADAS allows a detailed atomic modelling which, notably, takes into account the density dependence of both ionisation fractions and excitation coefficients according to the *generalised collisional radiative theory* (McWhirter & Summers 1984; Summers 1994, 2001). Such data have not generally been included in DEM analyses in the past, resulting in some confusion as to the interpretation of the real reasons for discrepancies found in these analyses.

The study carried out in Paper I also showed that spurious multiple peaks in the DEM distribution may derive from an inaccurate treatment of the population densities of the excited levels and ionisation fractions or from integral inversion techniques with arbitrary smoothing. Complex DEM structures, such as those proposed for solar and stellar coronae by several authors, have therefore been questioned.

Understanding *how* inhomogeneities combine to produce an observed mean emission measure is important for testing proposals for possible heating mechanisms. If the plasma is essentially in ionisation equilibrium and the radiative cooling and (or) conductive terms dominate(s) the energy balance, we expect the DEM to have everywhere the same shape, differing only by a roughly constant factor depending on the total amount of heating in that region. In this case, however, the distribution of the plasma in temperature depends mainly on its radiative and conductive properties and not on how and where the energy release has taken place. On the other hand, if the radiative cooling and (or) conduction are (is) not the dominant term in the energy balance, then the DEM will depend on how and where the heating has taken place and different structures may combine into a complex mean DEM distribution, such as one with multiple peaks. Furthermore, if the heating is impulsive, the plasma may not be in ionisation equilibrium and analysis methods based on emission measure become unreliable.

In this work we exploit the DEM in the spectral analysis of a quiet Sun area observed by SOHO-CDS and address the issue of how the DEMs of small subareas combine to give the DEM of a larger area. The relationship with bulk motion is also investigated. In Sect. 2 we give an overview of the observational data used in this work. In Sect. 3 we outline the reduction of such data. In Sect. 4 we discuss the DEM analysis performed on the observational data. We draw our conclusions in Sect. 5.

## 2. Overview of the CDS observing sequence

A full description of CDS scientific objectives and flight hardware is given by Harrison et al. (1995). Details pertinent to the observing sequence analysed in this paper are given in Brooks et al. (1999).

The data used for this work were taken using the NISAT\_S (ID 17 var. 2) observing sequence. This takes the full wavelength ranges from both the NIS channels, NIS-1 which covers the wavelength range 308–381 Å and NIS-2 which covers the range 513–633 Å. The 2 arcsec by 240 arcsec slit is used. This is the narrowest slit available, yielding the best spectral resolution. The sequence raster, covering an area of the Sun 20 arcsec by 240 arcsec, is made by moving the scan mirror to 10 adjacent locations each separated by 2.032 arcsec (less a contribution from solar rotation). The exposure time at each location is

50 s and the whole study takes 60 min to complete, including data transmission time from the spacecraft.

The observations used in this paper were made on 1996 December 5 at 06 h 58 m (UT) as CDS sequence s6011r00 which was also one of the datasets used by Brooks et al. (1999). We therefore take full advantage of the very detailed spectral analysis already carried out for this dataset. The pointing chosen was to the quiet Sun near Sun centre (see Brooks et al. 1999).

## 3. Data handling

### 3.1. Reduction of raw data

NIS detector data require debias correction, spectral rotation and line tilt correction, cosmic ray strike cleaning, drop-out detection, flat-fielding, correction for the localised “burn-in” of the detector by strong lines and correction for non-linearity in detector response. A discussion on the corrections applied to the raw data can be found in Brooks et al. (1999) (see also Lang et al. 2002). The reduction procedure has been reapplied to the raw data to take account of improved narrow slit burn-in and the wide slit burn-in correction (Lang et al. 2002). The spectral observations were fitted to Gaussian profiles by the program ADAS602 as described in Brooks et al. (1999).

### 3.2. Selection of subareas

In this study we sought to contrast the DEM from subregions of a raster with the DEM of the whole raster. To do so, we have chosen eight segments, each 40 pixels long in the  $y$ -direction (i.e. along the slit), in six of the exposures of the whole raster. Figures 1 and 2 show the O V (629.732 Å) and Mg IX (368.057 Å) intensity variation in the ten raster steps and then the position of the chosen segment of 40 pixels along all the pixels in its step. We have chosen some dark Mg IX (368.057 Å) regions (4(7L) and 6(8L)), regions around a narrow brightening (3(4), 5(7U), 7(8U) and 8(9)) and a more extended brightening (1(0) and 2(1)).

Figures 3 and 4 show the variation of the intensities of the O V (629.732 Å) and Mg IX (368.057 Å) lines along the slit. The dark regions show a rather flat intensity distribution along the slit, the extended bright regions a flattish distribution with higher counts than in the dark region, and the narrow brightening a peaked distribution with much higher counts.

### 3.3. Radiometric calibration

After fitting to Gaussian profiles, the radiometric calibration has been applied to the spectral observations following Lang et al. (2002) and references therein.

To the standard error in flux returned by the Gaussian fitting procedure ADAS602 (Brooks et al. 1999) we add, quadratically,  $\pm 8\%$  for aperture uncertainty,  $\pm 2\%$  for slit size uncertainty and  $\pm 10\%$  for burn-in correction for the line. Also added in the quadrature to the estimated standard error were the wavelength dependent uncertainties for the count/photon conversion. That is for NIS-1  $\pm 15\%$  below 368 Å and  $\pm 25\%$  above



**Fig. 1.** O V (629.732 Å) image of the chosen dataset (s6011r00). It shows on the left the ten raster steps and on the right the positions of the 8 segments each 40 pixels long alongside all the pixels of the relevant raster step. These are denoted as follows: the segment from step 0 as 1(0); the segment from step 1 as 2(1); the segment from step 4 as 3(4); the two segments from step 7 as 4(7L) for the lower one and 5(7U) for the upper one; the two segments from step 8 as 6(8L) for the lower one and 7(8U) for the upper one; the segment from step 9 as 8(9).

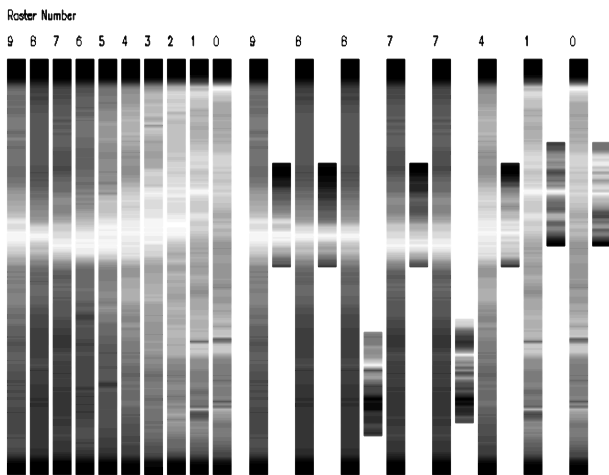


**Fig. 2.** Same as Fig. 1 for Mg IX (368.057 Å).

368 Å, for NIS-2,  $\pm 18\%$  at 584 Å and  $\pm 29\%$  at the ends of the band using linear interpolation between 584 Å and the ends of the band and for the NIS-2 2nd order,  $\pm 12\%$  at 303–304 Å.

## 4. DEM analysis

### 4.1. Method

The method used to derive the differential emission measure, the relevant part of the collisional-radiative theory for the line emissivity, most of the atomic data used and the evaluation of kernels have been discussed in detail in Paper I. To the atomic data used in Paper I, data for Mg IV, Al VII, Ar VII, and S V have been added from the CHIANTI 4 database (Dere et al. 1997; Young et al. 2003), and data for Ca VII and Ca VIII have

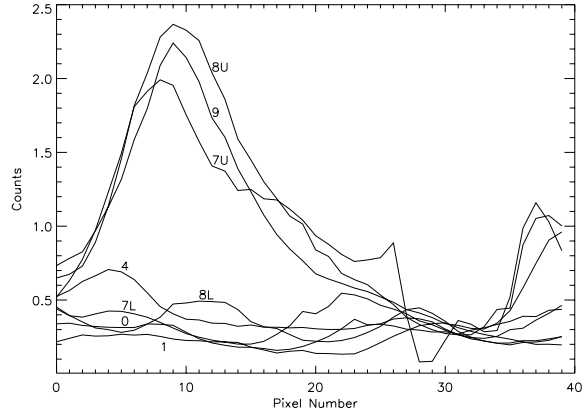


**Fig. 3.** Variation of intensity in the O V (629.732 Å) line along the slit for the 40 pixels long segments chosen.

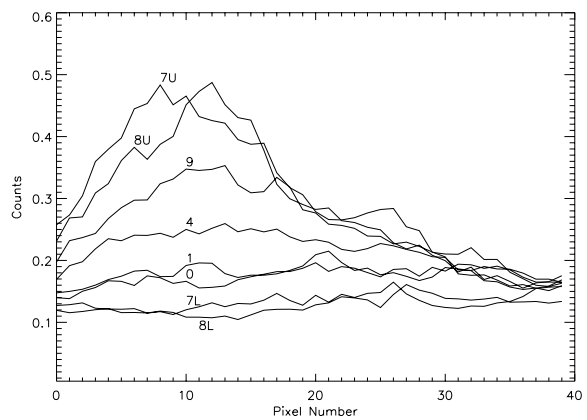


**Fig. 4.** Same as Fig. 3 for Mg IX (368.057 Å).

been taken from Landi & Bhatia (2003) and Landi et al. (2004), respectively.

The lines used in the integral inversion and in the evaluation of elemental abundances are indicated in Tables 1 and 5 with “i” (used in the integral inversion and evaluation of abundance) and “f” (compared with observations in the forward sense and used for the evaluation of elemental abundances). The selection of these lines follows from the considerations made in Sect. 4.2. Table 5, available at the CDS, contains the following information. Columns 1 and 2 list the element symbol and the ion charge ( $z + 1$ ), Col. 3 the adopted laboratory wavelength ( $\lambda^{\text{ad}}$ ), Col. 4 the reference for  $\lambda^{\text{ad}}$ , Cols. 5–8 the electronic configurations and terms, Col. 9 the peak temperature of line formation  $\log T_p$ , Col. 10 the observed wavelength, Col. 11 the theoretical intensity, Cols. 12 and 13 the observed intensity and the observational uncertainty, Col. 14 the chi-square  $(\sigma_0 \chi_i)^2$ , Col. 15 a note indicating whether the line has been used for the integral inversion “i” or compared in the forward sense “f”. Intensities in  $\text{erg cm}^{-2} \text{s}^{-1} \text{sr}^{-1}$  ( $\text{mW m}^{-2} \text{sr}^{-1}$  in SI units).

The DEM is evaluated separately for the mean spectrum and for each segment, adopting a constant electron density model for the evaluation of kernels as in Tables 3 and 4. A constant pressure model has also been considered, but, since the results are not appreciably different, this is not reported here. Anticipating the results of Sect. 4.2.3, Table 3 shows that the

**Table 1.** Lines used for the integral inversion and for evaluating the elemental abundances.  $\lambda^{\text{ad}}$  is our preferred laboratory wavelength and  $\lambda^{\text{cor}}$  the “corrected” observed wavelength in Brooks et al. (1999).  $T_p$  is the peak temperature of line formation. Since one line per ion at most is used in the integral inversion, we indicate with “i” the lines used in the integral inversion and “f” the lines compared with observations in the forward sense, i.e. by comparing the intensities predicted using the DEM with the observed intensities. The source for the adopted wavelength is denoted by E for Edlén (1983a,b, 1984, 1985a,b,c), F for Fawcett (1975), K for Kelly (1987), N for Martin et al. (1995), and O for Wiese (1985), respectively.

Ion	$\lambda^{\text{ad}}$	Transition	$\lambda^{\text{cor}}$	$\log T_p$	i/f
O III	525.797 <sup>N</sup>	$2s^2 2p^2 \ ^1D_2-2s 2p^3 \ ^1P_1$	525.801	4.95	f
O III	599.598 <sup>N</sup>	$2s^2 2p^2 \ ^1D_2-2s 2p^3 \ ^1D_2$	599.596	5.00	i
O IV	553.329 <sup>N</sup>	$2s^2 2p^2 P_{1/2}-2s 2p^2 \ ^2P_{3/2}$	553.343	5.20	f
O IV	554.076 <sup>N</sup>	$2s^2 2p \ ^2P_{1/2}-2s 2p^2 \ ^2P_{1/2}$	554.076	5.20	f
O IV	554.513 <sup>N</sup>	$2s^2 2p \ ^2P_{3/2}-2s 2p^2 \ ^2P_{3/2}$	554.512	5.20	f
O IV	555.263 <sup>N</sup>	$2s^2 2p \ ^2P_{3/2}-2s 2p^2 \ ^2P_{1/2}$	555.270	5.20	i
O IV	608.397 <sup>N</sup>	$2s^2 2p \ ^2P_{1/2}-2s 2p^2 \ ^2S_{1/2}$	608.312	5.20	f
Ne IV	543.886 <sup>E</sup>	$2s^2 2p^3 \ ^4S_{3/2}-2s 2p^4 \ ^4P_{5/2}$	543.881	5.30	i
O V	629.732 <sup>N</sup>	$2s^2 \ ^1S_0-2s 2p \ ^1P_1$	629.735	5.40	i
Ar VII	585.754 <sup>F</sup>	$3s^2 \ ^1S_0-3s 3p \ ^1P_1$	585.694	5.50	f
Ne V	359.375 <sup>E</sup>	$2s^2 2p^2 \ ^3P_2-2s 2p^3 \ ^3S_1$	359.374	5.50	i
Ne VII	561.72 <sup>E</sup>	$2s 2p \ ^3P_2-2p^2 \ ^3P_2$	561.725	5.70	i
Al VII	356.892 <sup>E</sup>	$2s^2 2p^3 \ ^4S_{3/2}-2s 2p^4 \ ^4P_{5/2}$	356.922	5.75	f
Ca VIII	582.845 <sup>K</sup>	$3s^2 3p \ ^2P_{1/2}-3s 3p^2 \ ^2D_{3/2}$	582.872	5.75	f
Ca X	557.759 <sup>E</sup>	$3s \ ^2S_{1/2}-3p \ ^2P_{3/2}$	557.764	5.80	i
Al VIII	328.183 <sup>E</sup>	$2s^2 2p^2 \ ^3P_2-2s 2p^3 \ ^3P_2$	328.249	5.90	f
Al VIII	328.230 <sup>E</sup>	$2s^2 2p^2 \ ^3P_2-2s 2p^3 \ ^3P_1$		5.90	f
Si VIII	316.218 <sup>E</sup>	$2s^2 2p^3 \ ^4S_{3/2}-2s 2p^4 \ ^4P_{3/2}$	316.215	5.90	f
Si VIII	319.839 <sup>E</sup>	$2s^2 2p^3 \ ^4S_{3/2}-2s 2p^4 \ ^4P_{5/2}$	319.840	5.90	f
Mg VIII	311.772 <sup>E</sup>	$2s^2 2p \ ^2P_{1/2}-2s 2p^2 \ ^2P_{3/2}$	311.750	5.90	f
Mg VIII	313.743 <sup>E</sup>	$2s^2 2p \ ^2P_{1/2}-2s 2p^2 \ ^2P_{1/2}$	313.758	5.90	i
Mg VIII	335.231 <sup>E</sup>	$2s^2 2p \ ^2P_{1/2}-2s 2p^2 \ ^2S_{1/2}$	335.233	5.90	f
Fe XI	352.661 <sup>O</sup>	$3s^2 3p^4 \ ^3P_2-3s 3p^5 \ ^3P_2$	352.671	6.05	f
Si IX	341.950 <sup>E</sup>	$2s^2 2p^2 \ ^3P_0-2s 2p^3 \ ^3D_1$	341.952	6.05	i
Al X	332.788 <sup>E</sup>	$2s^2 \ ^1S_0-2s 2p \ ^1P_1$	332.785	6.10	f
Al XI	550.04 <sup>E</sup>	$2s \ ^2S_{1/2}-2p \ ^2P_{3/2}$	550.050	6.15	f
Si X	347.408 <sup>E</sup>	$2s^2 2p \ ^2P_{1/2}-2s 2p^2 \ ^2D_{3/2}$	347.402	6.15	i
Fe XII	364.468 <sup>O</sup>	$3s^2 3p^3 \ ^4S_{3/2}-3s 3p^4 \ ^4P_{5/2}$	364.467	6.15	f
Si XII	520.662 <sup>E</sup>	$2s \ ^2S_{1/2}-2p \ ^2P_{1/2}$	520.685	6.30	i

electron density in the mean spectrum at the formation temperature of Mg VIII is approx.  $\log N_e = 7.7$ . In addition, Table 4 shows that the electron density in the 8 segments varies from  $\log N_e = 6.9$  to 8.3.

The evaluation of elemental abundances is performed independently for each segment and for the mean spectrum (see Sect. 4.4).

#### 4.2. Spectral analysis

A preliminary analysis using line intensity ratios is performed for selecting, for the integral inversion, lines not significantly affected by blending, and to infer the most likely electron density to be used in the evaluation of the  $G$ -functions. The selection is made with the aim of reducing, as much as possible, systematic errors due to the ubiquitous line blending. The spectral analysis of Brooks et al. (1999) is used as a starting point for lines and blends identification. Here we consider mainly lines to which I-codes A and B and P-codes 1 and 2 were assigned

and which are neither blended with lines of other ions nor affected by opacity. In the following, we indicate with  $R_{\text{th}}$  the theoretical line intensity ratio obtained with ADAS. The spectral analysis is then complemented with the DEM fit, which allows a detailed study of blends of different ions and a check of the results obtained from the line ratio analysis. For the aid of the reader in understanding why some of the lines were rejected from the DEM analysis in the subsequent sections, we note that the final DEM solution was found to be most reliable in the temperature range  $\log T_e = 5.0$  to 6.0. The results are given in Table 5 (available at CDS).

##### 4.2.1. Li-like sequence

Both lines of the Mg X  $2s^2S-2p^2P$  doublet (624.95 Å, 609.79 Å) were identified by Brooks et al. (1999), the  $1/2-1/2$  component being of code A[1] and the  $1/2-3/2$  component being blended with O IV which Brooks et al. estimated, from branching ratios, to contribute about 1/3 of the intensity

**Table 2.** Comparison between the Be-like Mg IX (368.057 Å) and the Li-like Mg X (624.95 Å) transitions in the selected segments.

Regions	segment	Li-like Mg X (624.95 Å)		Be-like Mg IX (368.057 Å)		note
		$I_{\text{th}}/I_{\text{obs}}$	$(\sigma_0\chi_i)^2$	$I_{\text{th}}/I_{\text{obs}}$	$(\sigma_0\chi_i)^2$	
Extended brightening	1(0)	1.1	1.3(-1)	0.5	3.4	
	2(1)	0.6	1.8	0.2	7.2	high velocities
Narrow brightening	3(4)	0.7	1.3	0.4	4.8	low intensities
	5(7U)	1.9	8.2	0.8	2.8(-1)	
	7(8U)	1.1	7.1(-1)	0.5	3.3	
	8(9)	2.5	2.5(+1)	1.0	1.4(-2)	
Dark regions	4(7L)	0.5	2.3	0.3	6.4	high velocities
	6(8L)	1.0	1.2(-4)	0.5	4.8	high velocities

of the blend. Good agreement is found with the DEM reconstruction in the mean spectrum. However, the DEM fails to reproduce the observed intensities in some segments, as shown in Table 2. This can be due to several reasons, including inaccuracies in the atomic data, a complex distribution of the plasma in electron density ( $N_e$ ), or to the DEM uncertainties which increase with temperature above  $\log T = 6.0$ . Another possible explanation could be that some uncertainties in the NIS-1/NIS-2 cross-calibration still exist, but this is ruled out by the considerations made in Sect. 4.5. Note, however, that when Mg X is reproduced by the DEM reconstruction, Mg IX (Be-like isoelectronic sequence, see next section and Table 2) is not and vice versa. Furthermore,  $I_{\text{th}}/I_{\text{obs}}$  for the Mg X lines is systematically higher than for the Mg IX line. As discussed in Sect. 4.2.2, the comparison with lines of Mg IX (Be-like) suggests that such discrepancies are likely to be caused by either some degree of non-equilibrium in the ionisation balance or a problem with the ionisation balance, e.g. by a recombination contribution to the  $2s\ 2p\ ^1P$  term of Mg IX or ionisation to it from e.g. the  $2s\ 2p^2\ ^4P$  term in the B-like Mg VIII, noting that as Mg VIII is used to construct the DEM, problems in that ion will not be identified.

The same doublet was identified for Al XI by Brooks et al. (1999), the  $1/2-3/2$  component at 550.04 Å and the  $1/2-1/2$  component at 568.16 Å blended with Ne V. The DEM reconstruction reproduces fairly well Al XI (550.04 Å) and predicts a 10% contribution to the blend with Ne V at 568.16 Å. Note, however, the large uncertainties in the DEM at the formation temperature of this line and in the Al abundance (see Sect. 4.4). Nevertheless,  $I_{\text{th}}/I_{\text{obs}}$  for the Al XI (550.04 Å) line is found to be systematically higher than for the Al X (332.788 Å) line (Be-like, see next section), which indicates the same systematic behavior found for the Mg X and Mg IX lines.

#### 4.2.2. Be-like sequence

O V (629.732 Å) is a strong NIS-2 calibration line and is used here both for selecting the subareas (Sect. 3.2) and for the integral inversion to sample the region around  $\log T = 5.4$ .

Brooks et al. (1999) identified the  $2s\ 2p^3P-2s\ 3s^3S$  transitions in C III, the 0-1 (538.080 Å) and the 1-1 (538.149 Å) blended together and with O II (537.832 Å), and the 2-1 (538.312 Å) blended with O II (538.262 Å) and O II (538.320 Å). Such blends may be affected by line opacities and their formation temperature is below the trusted temperature range for the DEM reconstruction ( $\log T \sim 4.75$  for O II and  $\log T \sim 4.95$  for C III). The results for these lines are therefore only indicative and are reported in Table 5.

The Ne VII  $2s\ 2p^3P-2p^2^3P$  multiplet has two lines known to be blended with Ne VI (1-2 at 558.60 Å and 1-0 at 562.98 Å). The other four have large error bars because of their low intensity, which does not allow a reliable line ratio analysis. The 561.38/559.95 Å ratio in the mean spectrum is 0.94 which, when compared with  $R_{\text{th}} = 0.75$ , may indicate a blend affecting the 561.38 Å line, although the large observational error bars do not allow a definitive conclusion. A similar consideration can be made for the 564.52 Å line, since the 564.52/559.95 Å ratio is 1.54 in the mean spectrum while  $R_{\text{th}} = 1.22$ . The Ne VII  $2s\ 2p\ ^1P_1-2p^2\ ^1S_0$  line at 561.27 Å could contribute to a blend with 561.38 Å; in this case the composite line ratio becomes essentially unity above  $N_e = 10^8\ \text{cm}^{-3}$  and shows a weak density dependence below such value, rising to 1.7 at  $N_e = 10^6\ \text{cm}^{-3}$ . Density sensitive ratios indicate only a lower limit to the electron density, which must be above  $\log N_e = 7$  to obtain line ratios consistent with the observations. Despite such uncertainties, we are forced to select, for the integral inversion, the strongest line apparently not affected by significant blending (2-2 at 561.72 Å) because of the lack of lines sampling the temperature region around  $\log T_e = 5.7$ . The DEM analysis does not confirm the blending of the lines at 561.38 Å and 564.52 Å, which are reproduced within the observational uncertainties, although the results are also compatible with the blending of the 561.38 Å and 561.27 Å lines. It indicates, instead, further blending for the lines at 558.60 Å and 562.98 Å or a problem in reproducing the Ne VI line intensities.

For the resonance line Mg IX (368.057 Å)  $I_{\text{th}}$  is about half  $I_{\text{obs}}$  in the mean spectrum. However, this line is reproduced within the observational uncertainties in segments 5(7U), 7(8U), and 8(9), i.e. in the segments around a narrow

brightening with higher intensities than average.  $I_{\text{th}}/I_{\text{obs}}$  is about 0.2–0.5 in the remaining segments (see Table 2). This may be due to a blend that occasionally affects this line, uncertainties in the extra burn-in correction for strong lines or DEM uncertainties which increase with temperature above  $\log T = 6.0$ . Uncertainties in the collisional excitation coefficients can obviously be another cause of the discrepancies. Note, however, that the situation is the opposite to that in the Li-like Mg X lines (Sect. 4.2.1). In fact, comparing the Li-like Mg X (624.95 Å) with the Be-like Mg IX (368.057 Å) in each segment we note that the ratio  $I_{\text{th}}/I_{\text{obs}}$  for the former is systematically higher than for the latter. This situation weakens the explanation of the discrepancies as due to occasional blends or uncertainties in the calibration of the instrument. Recombination to the  $2s\ 2p\ ^1P$  term or ionisation to it from e.g. the  $2s\ 2p^2\ ^4P$  term in the B-like Mg VIII could increase its population density and therefore increase the Mg IX (368.057 Å) intensity. Since Mg VIII is used to construct the DEM, problems in that ion will not be identified. However, level-resolved ionisation and recombination coefficients for Mg are not yet available and therefore this possibility cannot be checked. Such a systematic behaviour can also be interpreted as being due to an *overionisation* of the Li-like stage with respect to the equilibrium ionisation balance. This behaviour could appear evident in our analysis because of the use of Si lines in the calculation of the DEM at the formation temperatures of these lines ( $\log T \sim 6.0$  and above), which have relaxation time-scales for the ground states about 50% shorter than Mg at such temperatures (see Paper I). Mg IX (368.057 Å) was used in the integral inversion for the SERTS-89 AR spectrum (Paper I) and reproduced within the observational uncertainties.

The Al X  $2s^2\ ^1S_0-2s\ 2p\ ^1P_1$  transition at 332.788 Å was used in the integral inversion in Paper I and was found to be in excellent agreement with observation. Brooks et al. (1999) assigned code B[2] to this line since its position pattern was found not to be as consistent with temperature as expected. The DEM predicts an intensity much lower than observed. Note, however, the large uncertainties in the DEM at the formation temperature of this line and in the Al abundance (see Sect. 4.4). As noted in Sect. 4.2.1,  $I_{\text{th}}/I_{\text{obs}}$  for the Al XI (550.04 Å) line (Li-like) is found to be systematically higher than for the Al X (332.788 Å) line. This supports the conclusion drawn from the comparison between the Li-like Mg X (624.95 Å) and the Be-like Mg IX (368.057 Å) lines of an overionisation of the Li-like stage with respect to the equilibrium ionisation balance, but, as outlined for Mg IX, level-resolved ionisation balance calculations are needed to confirm this conclusion.

Of the Si XI transitions, the  $2s^2\ ^1S_0-2s\ 2p\ ^1P_1$  at 303.326 Å was identified by Brooks et al. (1999) in NIS-2 2<sup>nd</sup> order. Other Si XI lines analysed in Paper I are expected to be below the sensitivity of the instrument in a QS spectrum. The DEM reconstruction for the  $2s^2\ ^1S_0-2s\ 2p\ ^3P_1$  (580.92 Å) intercombination line yields a value 0.2 of the observed. Brooks et al. (1999) assigned I-code E to Si XI (604.12 Å) ( $2s\ 2p\ ^1P_1-2p^2\ ^1D_2$ ) because of its large wavelength difference with the  $\lambda^{\text{ad}}$ . Here it is predicted to have an intensity of only 0.06 erg cm<sup>-2</sup> s<sup>-1</sup> sr<sup>-1</sup> in the mean spectrum and therefore its identification in the QS in NIS-2 is rejected. For Si XI (303.326 Å) we find  $I_{\text{th}}/I_{\text{obs}} \sim 0.1$

in the mean spectrum and between 0.1 and 0.6 in the selected segments; the theoretical intensity is closer to observation (within  $1.5\sigma$ ) in segments 1(0), 2(1), 4(7L), 5(7U), and 6(8L). This discrepancy is consistent with the SERTS-89 spectral analysis of Paper I, where this line had  $I_{\text{th}}/I_{\text{obs}} \sim 0.5$ , and may at least partially be ascribed to the uncertainties of the QS DEM above  $\log T_e = 6.0$ . Possible blends are Fe XIII (303.320 Å) and S XIII (303.384 Å), but neither could contribute appreciably to the observed intensity. Note that this line may suffer from radiative pumping because of its close vicinity to the strong He II (303.78 Å). Possible uncertainties in the atomic data have been discussed by Lang et al. (2001). A more robust analysis of Si XI (303.326 Å) in NIS spectra could be done considering AR observations for which the DEM above  $\log T_e = 6.0$  is expected to be more reliable.

#### 4.2.3. B-like sequence

The observed O IV line ratios are not sensitive to density. Lines indicated as unblended by Brooks et al. (1999) form ratios in agreement with theory. The strongest line at 554.513 Å is selected for the integral inversion. O IV (609.829 Å) is blended with Mg X and, as discussed in Sect. 4.2.2, the DEM reconstruction is in good agreement with observation. The  $5/2-3/2$ ,  $3/2-3/2$ , and  $3/2-1/2$  components of the  $2s\ 2p^2\ ^2D-2p^3\ ^2P$  multiplet (616.952 Å, 617.005 Å, 617.036 Å) are reported as blended with O II. The discrepancies observed may be due to our difficulties in reproducing the O II lines, either because of opacity effects and/or because this line is formed below our trusted range of temperatures for the evaluation of the DEM.

All the  $2s^2\ 2p^2P-2s\ 2p^2S$  and  $2s^2\ 2p^2P-2s\ 2p^2P$  transitions in Mg VIII were classified as code B[1] by Brooks et al. (1999). The intensity ratio of lines sharing the same upper level shows that the 317.028/313.743 Å ratio is in excellent agreement with the theory ( $R_{\text{th}} = 0.64$ ). The 311.772/315.015 Å ( $R_{\text{th}} = 0.20$ ) and 338.983/335.231 Å ( $R_{\text{th}} = 1.26$ ) ratios, despite their theoretical values lying within the observational error bars, show systematic departures in the average spectrum and in the segments that may indicate that the 315.015 Å and 335.231 Å lines are affected by blends contributing 50% and 20% of the observed intensity, respectively. Correcting the average intensities using these estimates, we obtain a remarkable agreement in the electron density estimated by all the density sensitive Mg VIII line ratios (see Table 3). Mg VIII (311.772 Å) was reported as blended with Ni XV in Paper I, but this is expected to have negligible intensity in a QS spectrum. Mg VIII (315.015 Å) was selected for the integral inversion and reproduced within the observational uncertainties in Paper I, which may indicate that the blending is due to a line formed at temperatures below that of Mg VIII formation and becomes negligible compared with Mg VIII (315.015 Å) in AR conditions. Mg VIII (335.231 Å) is completely masked by Fe XVI (335.396 Å) in the SERTS-89 spectrum and Mg VIII (338.983 Å) was found in excellent agreement with observations in Paper I. We select Mg VIII (313.743 Å) for the integral inversion and the ratio 338.983/313.743 Å as density diagnostic at the temperature

**Table 3.** Electron density derived from Mg VIII lines ratios. The 315.015 Å and 335.231 Å line intensities have been corrected assuming that they are affected by blendings contributing 50% and 20% of the observed intensity, respectively.  $C$  is the correction factor applied to the line ratio to take blending into account.

Ratio (Å)	$\log N_e$	$C$
311.772/313.743	$7.7^{+0.3}_{-0.3}$	1.00
315.015/313.743	$7.8^{+0.3}_{-0.2}$	0.67
335.231/313.743	$7.8^{+0.5}_{-0.5}$	0.82
338.983/313.743	$7.8^{+0.5}_{-0.5}$	1.00
317.028/315.015	$7.7^{+0.3}_{-0.2}$	1.50
335.231/315.015	$7.7^{+0.7}_{-0.4}$	1.24
338.983/315.015	$7.8^{+0.9}_{-0.4}$	1.50
311.772/317.028	$7.7^{+0.3}_{-0.3}$	1.00
335.231/317.028	$7.7^{+0.5}_{-0.6}$	0.82
338.983/317.028	$7.7^{+0.6}_{-0.4}$	1.00

peak of line formation ( $\log T_p \approx 5.90$  K). The electron density in the selected segments, inferred from the 338.983/313.743 Å intensity ratio, is shown in Table 4. Given the reliability of this density diagnostic, such values are used for evaluating the  $G$ -functions. The DEM analysis confirms the conclusions drawn from the line ratio analysis. The 315.015 Å line is underestimated by 45% in the mean spectrum, lying outside the error bar, and systematically underestimated in all the segments, with  $I_{th}/I_{obs}$  between 0.2 (segment 2(1)) and 0.9 (segment 8(9)). The line at 335.231 Å is underestimated by 30% in the mean spectrum, lying outside the error bar, and systematically underestimated in all the segments, with  $I_{th}/I_{obs}$  between 0.4 (segments 2(1) and 4(7L)) and 0.8 (segment 5(7U) and 8(9)). Brooks et al. (1999) noted the absence of the Fe XVI  $3s^2 2p^2 P-3p^2 P$  lines at 335.396 Å and 360.743 Å which are bright in active region spectra (see also Paper I). The present analysis is consistent with the stronger 335.396 Å line blending with the Mg VIII (335.231 Å) line. Brooks et al. (1999) also indicated that the Fe XII (335.06 Å) line may be lost in the wings of the Mg VIII (335.231 Å) line. However, it should be noted that Lang et al. (2002) pointed out that for the Fe XVI doublet there could be extra wide-slit burn-in which is not accommodated by the analysis. This could affect the intensity of the Mg VIII (335.231 Å) line.

The Ne VI  $2s^2 2p^2 P-2s 2p^2 D$  transitions lie in the NIS-2 wavelength range. The  $1/2-3/2$  transition (558.591 Å) is blended with Ne VII. The  $3/2-3/2$  line (562.702 Å) is assumed to be blended with the  $3/2-5/2$  line (562.797 Å) and with Ne VII (562.98 Å). No useful ratio can therefore be formed with such lines. Table 5 shows that both blends are dominated by the Ne VI components which, however, are overestimated by 70–90% in the DEM reconstruction. Note that in the SERTS-89 spectrum (Paper I) the Ne VI  $2s^2 2p^2 P-2s 2p^2 P$  multiplet was reproduced within the observational uncertainties, but the  $2s^2 2p^2 P-2s 2p^2 S$  multiplet was overestimated by a factor of 2. This situation points to inaccuracies in the atomic data as the possible cause of the discrepancies. We are, nevertheless,

**Table 4.** Electron density derived from the Mg VIII 338.983/313.743 Å line ratio in the selected segments. The lower limit and the upper limit are indicated with “ll” and “ul”, respectively.

Segment	$\log N_e$
1(0)	$7.3^{+0.5}_{ll}$
2(1)	$6.9^{+0.6}_{ll}$
3(4)	$7.4^{+0.5}_{ll}$
4(7L)	$8.0^{+1.7}_{-0.6}$
5(7U)	$8.2^{ul}_{-0.6}$
6(8L)	$7.4^{+0.5}_{ll}$
7(8U)	$7.6^{+0.5}_{-0.9}$
8(9)	$8.3^{ul}_{-0.6}$

forced to use this multiplet to constrain the Mg/Ne abundance ratio (see Sect. 4.4), obtaining consistent results.

The Si x  $2s^2 2p^2 P-2s 2p^2 D$  lines are observed in the NIS-1 wavelength range, the  $3/2-3/2$  (356.054 Å) and  $3/2-5/2$  (356.029 Å) components being blended together. The composite line ratio obtained with this multiplet indicates  $N_e \approx 6 \times 10^8 \text{ cm}^{-3}$ , which is too high compared with the value obtained from Mg VIII. The DEM analysis indicates that further blending may affect these lines. However, they were *overestimated* in the SERTS-89 analysis, which suggests inaccuracies in the atomic data instead. The  $1/2-3/2$  component at 347.408 Å, which was in excellent agreement with observation in the SERTS-89 spectrum, is chosen for the integral inversion and is in good agreement with observation. These lines form in a temperature range where large uncertainties affect the DEM. Note that the temperature of line formation overlaps with that of Fe XII.

#### 4.2.4. C-like sequence

Brooks et al. (1999) assigned code A[1] to the  $2s^2 2p^2 {}^1D_2-2s 2p^3 {}^1D_2$  transition in O III at 599.598 Å, and to the  $2s^2 2p^2 {}^1D_2-2s 2p^3 {}^1P_1$  transition at 525.795 Å. The former is used here for the integral inversion and the latter is compared with observation in the forward sense. Both are reproduced within the observational uncertainties. O III at 597.818 Å ( $2s^2 2p^2 {}^1S_0-2s 2p^3 {}^1P_1$ ) was reported as blended with Ca VIII (597.851 Å) ( $3s^2 3p^2 P_{3/2}-3s 3p^2 D_{3/2}$ ) by Brooks et al. (1999), who estimated a 10% contribution by Ca VIII to the blend. This is confirmed by the DEM analysis which reproduces this blend within the observational uncertainties.

The O III  $2s^2 2p^2 {}^3P-2s^2 2p 3s {}^3P$  transitions were identified in NIS-1 by Brooks et al. (1999) at  $\lambda^{cor} = 373.804$  Å (1–2 code C[3]), 374.097 Å (0–1, 2–2 and 1–1, code B[1]), and 374.433 Å (1–0 and 2–1, code B[2]). The relative intensities of the lines were found in accord with expectation and are density insensitive. These lines were found in good agreement with observations in the SERTS-89 spectrum (Paper I). The DEM reconstruction in the mean CDS spectrum and in the individual segments is, however, lower than observations ( $I_{th}/I_{obs} \sim 0.2$ ). Given also the good agreement found with O III (599.598 Å) and O III (525.795 Å), we explored the possibility that such discrepancies may be due to inaccuracies in the NIS-1/NIS-2 cross

calibration. We found, however, that the correction required to bring these lines into agreement would be well above the estimated uncertainties in the cross calibration (see Lang et al. 2002; and Sect. 4.5) and therefore the reason for such discrepancy remains unclear.

The Ne V  $2s^2 2p^2 \ ^3P-2s 2p^3 \ ^3D$  transitions are observed in NIS-2 as a blend of the 2–3 and 2–2 components (572.334 Å, 572.112 Å), a blend of the 1–1 and 1–2 components (569.758 Å, 569.836 Å) and a blend of the 0–1 component (568.421 Å) with Al XI. The ratio formed with the 2–3 plus 2–2 composite assembly and the 1–1 plus 1–2 is density insensitive and in agreement with theory. This multiplet is overestimated by the DEM reconstruction by at least 60%. A comparison with other Ne V lines points to uncertainties in the atomic data as a possible cause for the discrepancies, but we note that the DEM at the formation temperature of these lines is mainly constrained by the Ne V (359.375 Å) line whose choice is mainly supported by the lack of other unblended lines in the temperature range rather than by a line ratio analysis (see below). The fact that our analysis overestimates these NIS-2 Ne V lines while using a NIS-1 Ne V line to constrain the DEM would point also, as discussed above for O III, to a possible inaccuracy of the NIS-1/NIS-2 cross-calibration, but this is excluded as above.

Of the Ne V  $2s^2 2p^2 \ ^3P-2s 2p^3 \ ^3S$  transitions, observed in NIS-1, the 0–1 (357.946 Å) is thought to be blended with Ne IV and the 1–1 (358.476 Å) with Fe X. The remaining line (2–1 at 359.375 Å) was classified as code B[2] and was used in the wavelength calibration. This line is also selected here for the integral inversion, although no line ratio can support this choice, which is cross-checked after the DEM runs. Brooks et al. (1999) noticed that the 357.946/359.375 Å intensity ratio does not agree with theory, which they interpreted as due to the blending of the Ne V (357.946 Å) line with Ne IV. Also they outlined that the position patterns are not a perfect match to either Ne V or Ne IV, casting a slight doubt on the identifications. The DEM reconstruction underestimates this blend ( $I_{th}/I_{obs} \sim 0.6$ ), supporting the possibility that a further line may contribute to the observed intensity. In Paper I it was suggested that the blend of Ne V and Ne IV in the SERTS-89 spectrum was unlikely both because the unblended Ne IV line is in good agreement with observation and because our adopted laboratory wavelengths indicate a separation above the resolution of the instrument. Brooks et al. (1999) found that the position pattern of Ne IV (358.476 Å) has large error bars and is more typical of the temperature of Fe X. We find that the Fe X contribution is 10% and this blend is reproduced just above the observational error bars. An examination of the wavelength shifts in individual segments reveals some inconsistencies between Ne V (357.946 Å) and Ne V (359.375 Å) (especially in segment 3(4) where the former is  $-0.26$  Å away from the laboratory wavelength) and between Ne V (358.476 Å) and Ne V (359.375 Å) (especially in segment 4(7L) where the former is  $0.26$  Å away from the laboratory wavelength). Ne V (359.375 Å), on the other hand, does not reveal shifts larger than  $0.1$  Å, which supports our identification. Such a situation suggest the presence of unidentified lines contributing to the blend with Ne V (358.476 Å) and Ne V (357.946 Å)

produced possibly from lower temperature plasma, given the agreement found in the SERTS-89 active region spectrum. The  $2s^2 2p^2 \ ^1D-2s 2p^3 \ ^1P$  transition (365.599 Å) is thought to form a blend with Fe X, which Brooks et al. (1999) found consistent with the position pattern which is a mixture of lines of different temperature. The DEM reconstruction is in good agreement with observation.

The  $2s^2 2p^2 \ ^3P-2s 2p^3 \ ^3D$  transitions in Si IX were also observed in the NIS-1 wavelength range. The 1–1 and 1–2 components ( $\lambda^{ad} = 344.954$  Å and  $345.120$  Å) form a blend at  $345.104$  Å and the 2–1, 2–2 and 2–3 ( $\lambda^{ad} = 349.620$  Å,  $349.791$  Å and  $349.860$  Å) another at  $\lambda^{cor} = 349.856$  Å. Brooks et al. (1999) found that these 3 components have the same position patterns which fall in the correct temperature class, with appropriate relative intensities. All observed Si IX lines were found in good agreement with observations in the SERTS-89 spectrum (Paper I). The only unblended component (0–1 at  $341.950$  Å) was assigned code B[1] by Brooks et al. (1999) and is chosen here in the integral inversion to sample the region around  $\log T = 6.05$ . Nevertheless, the two blends are underestimated by the DEM, which is strikingly in contrast with the results of Paper I and Brooks et al. (1999). We note that the composite ratios are dependent on density below  $\log N_e = 9$ . In the mean spectrum they would indicate  $N_e \sim 2 \times 10^8 \text{ cm}^{-3}$ , which is not consistent with the electron density inferred from Mg VIII. Therefore, in this case the discrepancies could be due to uncertainties in the dependence of the population densities on density or to density inhomogeneities which are not accounted for in the method used. Since this problem is not present at higher densities, i.e. in the SERTS-89 active region, the former explanation is preferred. The region of formation overlaps both with Mg X and Fe XI.

The  $2s^2 2p^2 \ ^1D_2-2s 2p^3 \ ^1D_2$  transition in Mg VII (319.018 Å) was identified by Brooks et al. (1999) with a good position pattern typical of its temperature. This line may be blended with Ni XV, but the SERTS-89 analysis in Paper I could not give a definite answer on the relative contributions because of the high density sensitivity of the Mg VII transition. Its intensity in the CDS spectrum is underestimated by the DEM, but a significant contribution from Ni XV seems unlikely in a QS spectrum. For Mg VII, the  $2s^2 2p^2 \ ^3P-2s 2p^3 \ ^3P$  transitions also lie in the NIS-1 wavelength range. Brooks et al. (1999) identified the 0–1 component ( $363.749$  Å), the 1–0 ( $365.162$  Å), 1–2 ( $365.221$  Å) and 1–1 ( $365.234$  Å) components blended together, and the blend of the 2–2 ( $367.658$  Å) and 2–1 ( $367.671$  Å) components, resulting in three lines of code C[1], B[1], and A[1], respectively, with the same position pattern. The analysis of Paper I overestimated these lines, outlining possible inaccuracies in the atomic data. The present analysis supports such conclusions as it overestimates the mean intensities by a factor of 2. We note also that the composite line ratios are density sensitive below  $\log N_e = 8$ , but both observed ratios are at the Boltzmann limit or slightly above.

Al VIII  $2s^2 2p^2 \ ^3P-2s 2p^3 \ ^3P$  transitions were identified by Brooks et al. (1999) in the NIS-1 spectrum as a blend of the 1–0 ( $325.280$  Å), 1–2 ( $325.296$  Å) and 1–1 ( $325.343$  Å) components, and a blend of the 2–2 ( $328.183$  Å) and 2–1 ( $328.230$  Å) components. The 0–1 component was not observed,

as expected since its intensity is below the sensitivity of the instrument. We are unable to produce a reliable Gaussian fit of the 1–0, 1–2, 1–1 blend in the spectra analysed while the 2–2, 2–1 blend is underestimated by the DEM analysis. Note, however, the large uncertainties in the Al abundance (see Sect. 4.4).

#### 4.2.5. N-like sequence

The O II  $2s^2 2p^3 \ ^2D-2s 2p^4 \ ^2P$  multiplet was identified with the 3/2–1/2 component at 537.832 Å blended with C III and the 5/2–3/2 (538.262 Å) and the 3/2–3/2 (538.320 Å) components blended together and with C III. As discussed in Sect. 4.2.2, such blends may be affected by line opacities and their formation temperature is below the trusted temperature range for the DEM reconstruction. For these reasons and because of a lack of suitable atomic data, the  $2s^2 2p^3 \ ^4S-2s^2 2p^2 3s \ ^4P$  lines at 539.086–539.854 Å are not discussed here. The  $2s^2 2p^3 \ ^2D-2s^2 2p^2 3s \ ^2P$  lines are identified as a blend of the 5/2–3/2 (616.303 Å) and the 3/2–3/2 (616.379 Å) components and a contribution of the 3/2–1/2 (617.063 Å) component to a O IV blend. The former is underestimated by the DEM and the latter gives a negligible contribution to the O IV blend.

The Ne IV  $2s^2 2p^3 \ ^2D-2s 2p^4 \ ^2P$  and  $2s^2 2p^3 \ ^4S-2s 2p^4 \ ^4P$  transitions are observed. The  $2s^2 2p^3 \ ^2D-2s 2p^4 \ ^2P$  lines (NIS-1) are blended with other ions, the 3/2–1/2 (357.825 Å) with Ne V (see Sect. 4.2.4) and the 5/2–3/2 (358.688 Å) and 3/2–3/2 (358.746 Å) with Fe XI, and are therefore excluded from the line ratio analysis. Both are underestimated by the DEM, which indicates the presence of further blends. Young et al. (1998) suggested a contribution from Si XI and Fe XIV to the blend with the 5/2–3/2 and 3/2–3/2 components. Since the contribution of Si XI is found to be negligible, and Fe XIV is not expected to give a significant contribution to the observed intensity in a QS spectrum, this suggestion cannot be confirmed. The  $2s^2 2p^3 \ ^4S-2s 2p^4 \ ^4P$  transitions (541.126 Å, 542.070 Å, 543.886 Å), observed in NIS-2, are sensitive insensitive and form ratios in agreement with theory. The Ne IV (543.886 Å) line was used in the Brooks et al. (1999) wavelength calibration and it is selected here for the integral inversion. Good agreement is found in the DEM analysis as well. This situation could support the possibility that the discrepancies found for the  $2s^2 2p^3 \ ^2D-2s 2p^4 \ ^2P$  lines may be due to inaccuracies in the NIS-1/NIS-2 cross calibration as discussed in Sect. 4.2.4 for the C-like O III  $2s^2 2p^2 \ ^3P-2s^2 2p 3s \ ^3P$  multiplet. This latter possibility is contemplated because, as for the C-like case, the region of formation is constrained by a Ne IV NIS-2 line. As for the C-like case, this is ruled out (see Sect. 4.5).

The  $2s^2 2p^3 \ ^2D-2s 2p^4 \ ^2D$  multiplet in Mg VI (349.108–349.179 Å) lies unresolved in the NIS-1 wavelength range and is reported by Brooks et al. (1999) as blended with a Fe XI line. However, the resulting position pattern did not resemble either of the two ions, which resulted in assigning code B[2] to this blend. The analysis of Paper I overestimated this blend and it was suggested that, because of fitting problems, only two of the four Mg VI multiplet components were actually measured. The present DEM analysis

of the CDS spectrum overestimates this multiplet as well and, given the lower resolution of the CDS instrument, the explanation that only two components were actually fitted is no longer sustainable. Given also the discrepancies in the position pattern, the likely explanation seems now that the atomic data for Mg VI are in error. Nevertheless, we are forced to use this multiplet to constrain the Mg/Ne abundance ratio (see Sect. 4.4), obtaining consistent results.

The  $2s^2 2p^3 \ ^4S-2s 2p^4 \ ^4P$  multiplet in Al VII lies in the NIS-1 wavelength range and the identification of its components was discussed by Brooks et al. (1999). The strongest 3/2–5/2 component (356.892 Å) was identified by Brooks et al. (1999) with a position pattern that could indicate a weak unknown blend and led to the assignment of code C[2]. The DEM reconstruction overestimates this line by 40%. The 3/2–3/2 component (353.777 Å) is thought to be blended with Fe XIV. The position pattern for this blend is more like that of the Fe XIV line formation temperature. Scaling from the 3/2–5/2 component of the Al VII multiplet, Brooks et al. (1999) estimated, however, that the Fe XIV contribution should be about a third of the total intensity. We are unable to produce a reliable Gaussian fit of this multiplet, but the DEM reconstruction predicts a Fe XIV contribution of about 1/5. The weakest 1/2–1/2 component (352.159 Å) is expected to contribute a few percent of a blend with Fe XII and Mg V. This is confirmed by the DEM reconstruction and good agreement is found for this blend (see Sects. 4.2.6 and 4.2.5).

The  $2s^2 2p^3 \ ^4S-2s 2p^4 \ ^4P$  transitions in Si VIII lie in the NIS-1 wavelength range. All three lines are observed in the expected flux ratio. The 3/2–3/2 and 3/2–5/2 lines (316.218 Å, 319.839 Å) have code A[1] and were used in the Brooks et al. (1999) wavelength calibration. The DEM reconstruction reproduces these lines, including the 3/2–1/2 component at 314.356 Å, within the observational uncertainties. The region of formation overlaps with Mg VIII which is used for the integral inversion.

#### 4.2.6. O-like sequence

The Mg V  $2s^2 2p^2 \ ^3P-2s 2p^5 \ ^3P$  multiplet lies in the NIS-1 wavelength range. The 2–2 component (353.092 Å) is expected to be the strongest. Thomas & Neupert (1994) identified five of the six lines, the 1–0 component not being reported. The 1–1 line was indicated as blended with Na VII. The analysis of the SERTS-89 data carried out in Paper I overestimated the 1–0 and 2–2 components, and reproduced the other four within the observational uncertainties. Brooks et al. (1999) indicated that the 1–0 line (352.197 Å) is dominated primarily by an Fe XII line (used in the wavelength calibration) as reflected in the position pattern and intensity, and indicated a further blend with Al VII. They also indicated that the 0–1 line (354.221 Å) is more intense than expected and could be blended. They ruled out a possible blend of the 1–1 component with Na VII. For the unblended lines the position patterns show large error bars so that these identifications were indicated as not secure. In the analysis carried out here, only the blend at  $\lambda^{\text{obs}} = 352.089 \text{ \AA}$  is considered since the other Mg V lines are too weak to be

fitted reliably. Good agreement is found, confirming the blend with Fe XII and Al VII. The expected intensities for the other transitions of this multiplet are reported in Table 5.

#### 4.2.7. F-like sequence

Brooks et al. (1999) identified the  $2s^2 2p^5 2P-2s 2p^6 2S$  doublet in Mg IV. The  $1/2-1/2$  component (323.309 Å) is too weak to be fitted reliably in our spectra and it is predicted to have an intensity of  $0.8 \text{ erg cm}^{-2} \text{ s}^{-1} \text{ sr}^{-1}$  in the mean spectrum. The  $3/2-1/2$  component (320.995 Å) is blended with Fe XIII and their intensities are reproduced within the observational uncertainties.

#### 4.2.8. Na-like sequence

Brooks et al. (1999) assigned code B[1] to both lines of the  $3s^2 S-3p^2 P$  transition in Ca X (557.759 Å, 574.007 Å). Their ratio in the average spectrum is 1.5, which may indicate a weak blend affecting the 574.007 Å line since  $R_{\text{th}} = 1.9$ . The stronger line was used by Brooks et al. (1999) in the wavelength calibration and it is used here for the integral inversion. The DEM reconstruction underestimates the 574.007 Å line, except in segments 4(7L), 5(7U) and 7(8U) where it is reproduced within the observational uncertainties, supporting the case of blending affecting this line.

Regarding the  $3p^2 P-3d^2 D$  multiplet in Ar VIII, we fit the  $1/2-3/2$  (519.464 Å) and  $3/2-5/2$  (526.496 Å) components as in Brooks et al. (1999). The  $3/2-3/2$  component (526.893 Å) is predicted to have negligible intensity, consistent with the observation. The  $1/2-3/2$  (519.464 Å) predicted intensity is only 12% of the observed intensity, and therefore its identification is doubtful. The DEM reconstruction for the  $3/2-5/2$  (526.496 Å) component is 50% lower than observed.

#### 4.2.9. Mg-like sequence

For this sequence, we consider the identification of S V (518.299 Å) ( $3s 3p^1 P_1-3s 4s^1 S_0$ ) and Ar VII (585.754 Å) ( $3s^2 1S_0-3s 3p^1 P_1$ ). For the former we obtain  $I_{\text{th}}/I_{\text{obs}} \sim 0.15$ . Note that the S abundance is taken from Feldman et al. (1992) since no reliable estimate can be made with the data at hand, and that S V (518.299 Å) lies close to the lower limit of the wavelength range of the NIS-2 detector. Ar VII (585.754 Å) is reproduced within the observational uncertainties.

#### 4.2.10. Al-like sequence

Brooks et al. (1999) identified the  $1/2-3/2$  and  $3/2-5/2$  components of the  $3s^2 3p^2 P-3s 3p^2 2D$  multiplet in Ca VIII (582.845 Å and 596.935 Å). We are unable to obtain a reliable Gaussian fit to the 596.935 Å line, but good agreement is found with the observed  $1/2-3/2$  (582.845 Å) component. The  $3/2-3/2$  component (597.851 Å) is found to contribute 15% to a blend with O III.

The  $1/2-3/2$  and  $3/2-5/2$  components of the same multiplet in Fe XIV were identified, the latter indicated as blended with Al VII. We were unable to obtain reliable fits to the

observed lines in the set analysed here, but we predict a negligible contribution to the blend with Al VII. The predicted intensity for the strongest component ( $1/2-3/2$  at 334.178 Å) is only  $1.2 \text{ erg cm}^{-2} \text{ s}^{-1} \text{ sr}^{-1}$ . In Paper I severe problems were found in the atomic data for Fe XIV, but these cannot be addressed here because of the weakness of these lines in our QS spectra.

#### 4.2.11. Si-like sequence

Lines of the Fe XIII  $3s^2 3p^2 3P-3s 3p^3 3D$  multiplet were identified by Brooks et al. (1999). The blend of the  $2-2$  and  $2-1$  components is predicted to be much weaker than observed, and therefore we do not confirm their identification at  $\lambda^{\text{cor}} = 372.131 \text{ Å}$ . The  $0-1$  component, identified at  $\lambda^{\text{cor}} = 348.148 \text{ Å}$ , is overestimated by 50% and therefore we cannot confirm the Brooks et al. (1999) suggestion that this line has an unknown blend. The blend of the  $1-2$  and  $1-1$  components, identified by Brooks et al. (1999) at  $\lambda^{\text{cor}} = 359.777 \text{ Å}$ , is reproduced within the observational uncertainties.

The Fe XIII  $3s^2 3p^2 3P-3s 3p^3 3P$  multiplet was also considered by Brooks et al. (1999). The strongest component is the  $1-1$  (312.095 Å) which we predict to have an intensity of  $3.5 \text{ erg cm}^{-2} \text{ s}^{-1} \text{ sr}^{-1}$  in the mean spectrum considered here, and was not detected by Brooks et al. (1999). The  $2-1$  component (321.394 Å) was identified at  $\lambda^{\text{cor}} = 321.436 \text{ Å}$  and is here predicted to have an intensity of  $1.8 \text{ erg cm}^{-2} \text{ s}^{-1} \text{ sr}^{-1}$  in our mean spectrum although we were unable to obtain a reliable fit to the observed line because it is too weak. The  $2-2$  component (320.800 Å) contributes 15% of the intensity of the blend with Mg IV, which is reproduced within the observational uncertainties. The  $1-2$  component (311.552 Å), identified by Brooks et al. (1999) at  $\lambda^{\text{cor}} = 311.476 \text{ Å}$ , is predicted to have negligible intensity in our mean spectrum. Note that lines of Fe XIII were systematically underestimated in Paper I, which was ascribed to uncertainties in the atomic modelling for Fe.

Lines of Ca VII were also identified by Brooks et al. (1999), but we could not obtain reliable Gaussian fits and report the predicted intensities only in Table 5.

#### 4.2.12. P-like sequence

Lines of Fe XII are observed in the NIS-1 wavelength range. Brooks et al. (1999) assigned code A[1] to the unblended Fe XII (364.468 Å) line ( $3s^2 3p^3 4S_{3/2}-3s 3p^4 4P_{5/2}$ ). The DEM reconstruction of this line is within the observational error bars. The other components of the multiplet,  $3/2-1/2$  at 346.852 Å and  $3/2-3/2$  at 352.107 Å, have codes B[2] and B[1], respectively. The 352.107 Å line was reported as blended with Mg V and Al VII. The predicted intensities for the  $3/2-1/2$  (346.852 Å) line and for the blend of the  $3/2-3/2$  (352.107 Å) component with Mg V and Al VII are in good agreement with observations. The 346.852/364.468 Å ratio, which is density insensitive, is in good agreement with theory. The DEM reconstruction for these lines is also in good agreement with observations. Brooks et al. (1999) identified also the  $3s^2 3p^3 2D_{5/2}-3s 3p^4 2D_{5/2}$  (338.263 Å) line. The DEM analysis, however, does not confirm the identification since it

predicts an intensity a factor 10 weaker than observed. The region of formation overlaps with Si X.

#### 4.2.13. S-like sequence

All components of the  $3s^2 3p^4 \ ^3P-3s 3p^5 \ ^3P$  multiplet in Fe XI were identified in Brooks et al. (1999) and the 2–2 component (352.661 Å) was used in the wavelength calibration (code A[2]). The 1–0 component (349.046 Å) is blended with Mg VI, but, according to the DEM reconstruction, the Fe XI contribution to the intensity is negligible. The 0–1 component (358.621 Å) is blended with Ne IV, but further blending is required to match the observed intensity. The Si XI line at 358.656 Å is found to have negligible contribution to this blend in QS conditions. A possible blend with an unknown component was suggested by Brooks et al. (1999) for the 2–1 component at 341.113 Å. We find the 356.519/352.661 Å and 369.154/352.661 Å line ratios in agreement with theory, but the 341.113/352.661 Å line ratio is approximately a factor 2.7 too high, which confirms the blending of the 341.113 Å line. The DEM analysis supports such conclusions too. The contribution of the Fe XIII line at 356.59 Å is found to be negligible. The region of formation overlaps with Si IX and Mg XI.

#### 4.2.14. Cl-like sequence

The Fe X  $3s^2 3p^5 \ ^2P_{3/2}-3s 3p^6 \ ^2S_{1/2}$  transition at 345.723 Å has code A[1] in Brooks et al. (1999) and was used in the wavelength calibration. Good agreement is found with the DEM reconstruction. The other component of the multiplet, the 1/2–1/2 at 365.543 Å, is blended with Ne V. The DEM reconstruction for this blend is in good agreement with observation. The line at  $\lambda^{\text{cor}} = 358.424$  Å was considered to be a blend of Ne V and the  $3s^2 3p^4 3d \ ^4F_{9/2}-3s 3p^5 3d \ ^4F_{9/2}$  Fe X transition by Brooks et al. (1999). The DEM analysis indicates that the Fe X contribution to this blend is 10%. The temperature of formation of Fe X overlaps with Mg IX. Note that Fe X lines were systematically underestimated in Paper I, which was attributed to an inaccurate treatment of the ionisation/recombination balance.

### 4.3. The mean DEM and the DEM from individual segments

The intensities of the lines selected for the integral inversion in each segment are compared with the mean intensity in Fig. 5. Also in Fig. 5 we compare the line shift with respect to the average spectrum for each segment. Line intensities in the transition region tend to be lower than average when velocities of the order of 30 km s<sup>-1</sup>, either as upflows or downflows, are present. In segments 1(0), 2(1), 4(7L), and 6(8L) velocities of the order of 50 km s<sup>-1</sup> are present. In such conditions the plasma can travel a hydrostatic scale-height in 300 s at log  $T = 5.5$ . This is an order of magnitude shorter than the relaxation time-scales for the ground states of Ne, Mg, Si, and S at the inferred electron densities (see Paper I) and therefore we expect ionisation equilibrium to break down in such regions. Note, however, that the relaxation time-scales for ground

levels presented in Paper I are evaluated directly from the ionisation/recombination cross-sections. The time required to reach ionisation equilibrium can be much shorter than these values if departures are small. Hydrodynamic calculations (see, e.g., Spadaro et al. 2003; Lanza et al. 2001) indicate that such departures for a single loop may last only for short times and may be not too large.

The DEM from the mean spectrum and from the selected segments are shown in Fig. 6. Above log  $T = 6.0$  the DEM is less reliable because of the weakness of the lines in the quiet Sun. The ratios of each segment's DEM with the mean spectrum DEM (lower panels of Fig. 6) show that the distribution of the plasma in temperature is essentially the same in all segments except those around the extended brightening (1(0) and 2(1)). These latter are the regions with the lowest electron density which also show *downflow* velocities of the order of 50 km s<sup>-1</sup> (Fig. 5) and are expected to contain plasma not in ionisation equilibrium. It is not possible, therefore, to establish whether the different DEM shape is real or due to a breakdown of the assumption of ionisation equilibrium. If real, such a shape may suggest that the two extended Mg IX brightening segments correspond to the top of systems of extended loops whose footpoints are outside the selected segments. In this case, transition region lines may form in compact loops which do not reach coronal temperatures and are thermally decoupled from the plasma emitting in Mg IX. Such compact loops are known to show high velocities (see, e.g., Lanzafame et al. 1999). Interestingly, the DEM for segment 4(7L), which correspond to a Mg IX dark region with  $N_e \approx 10^8$  cm<sup>-3</sup>, does not show evident deviations in the DEM shape, despite *upflow* velocities of the order of 50 km s<sup>-1</sup> being present.

There are other possible indications of deviations from ionisation equilibrium. Comparing the Li-like Mg X (624.95 Å) with the Be-like Mg IX (368.057 Å) in each segment (as well as the Li-like Al XI (550.04 Å) with the Be-like Al X (332.788 Å), see Sects. 4.2.1 and 4.2.2) we have shown that the ratio  $I_{\text{th}}/I_{\text{obs}}$  for the former is systematically higher than for the latter. Such a systematic behaviour can be interpreted as being due to an *overionisation* of the Li-like stage with respect to the equilibrium ionisation balance. It is expected that this behaviour appears evident in our analysis because of the use of Si lines in the calculation of the DEM at the formation temperatures of these lines (log  $T \sim 6.0$  and above), which have relaxation time-scales for the ground states 50% shorter than those of Mg at such temperatures (see Paper I). In this case, in fact, any effect which is dependent on the ionisation/recombination rates of elements with longer relaxation time-scales than Si would become detectable. The Mg X (624.95 Å)/Mg IX (368.057 Å) line intensity ratio is not correlated with line shifts and this could be considered an evidence against non-equilibrium conditions. It can be expected, however, that small scale events could cause some degree of non-equilibrium in the corona without producing bulk flow of plasma and therefore measurable line shifts. As discussed in Sects. 4.2.1 and 4.2.2, an alternative explanation is that recombination to the  $2s 2p \ ^1P$  excited term of the Be-like ions or ionisation to it from e.g. the  $2s 2p^2 \ ^4P$  term in the B-like ions give a contribution which is not accounted for

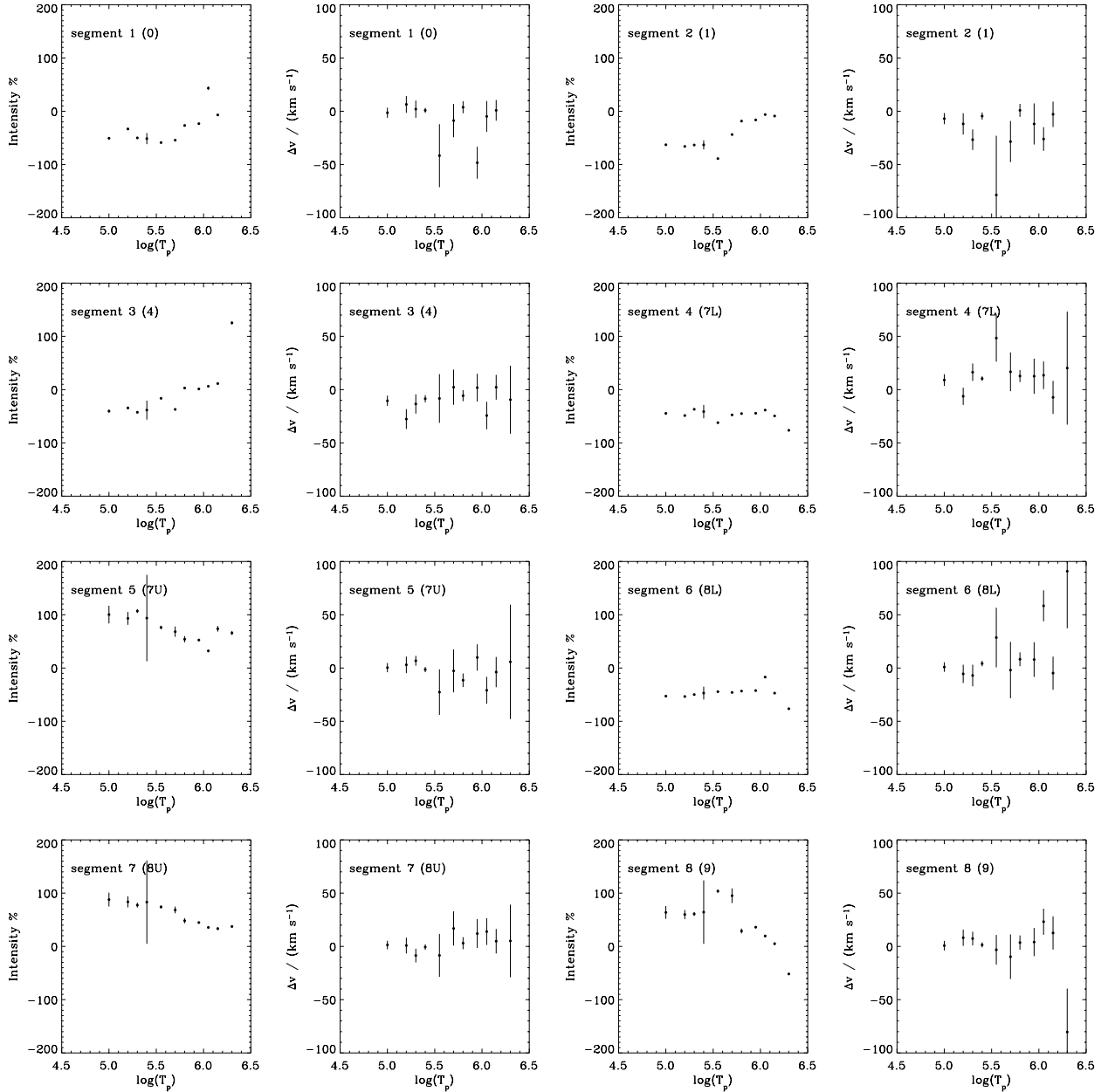


**Fig. 5.** Intensity variation compared to the mean spectrum and wavelength shift in velocity units with respect to the mean spectrum of the lines selected for the integral inversion in each segment. Error bars are evaluated combining the measurement errors as in Sect. 3.3. Data points with no bars have uncertainties below the size of the symbols. Note that in segments 1(0) and 2(1) we are unable to obtain a reliable Gaussian fit of the Si XII (520.662 Å) and therefore this line is not reported for such segments.

in our analysis since level-resolved ionisation balance calculations for Mg and Al are not yet available.

#### 4.4. Elemental abundances

In evaluating elemental abundances, we start by assuming that the Ne abundance (with respect to H) in the transition region and corona is the same as in the photosphere. In other words, we assume that high-FIP elements (i.e. elements with their first ionisation potential – FIP – greater than approximately 10 eV) have coronal abundances close to their photospheric values. This assumption is necessary since we are unable to obtain

elemental abundances relative to H using the CDS-NIS spectrum alone, and therefore our abundances must be taken relative to one of the elements emitting in the CDS-NIS spectrum. Alternatively, we could have assumed, without loss of validity of our results, that low-FIP elements have photospheric abundances and that high-FIP elements are depleted in the corona. In this latter case, all abundances would have been scaled by a constant factor (approximately from the higher dotted line to the lower in Fig. 7) and the DEM would have been multiplied by the same factor.

We have selected all observed lines emitted by ions other than Ne which do not show evident blending or problems in

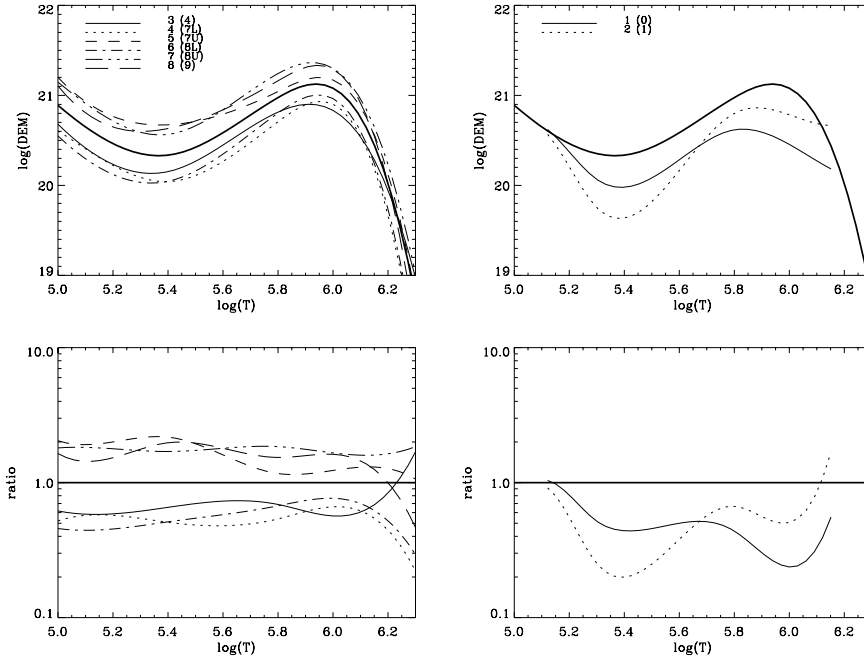


**Fig. 6.** DEM from the selected segments compared with the mean spectrum (thick solid line). Above  $\log T = 6.0$  the DEM is less reliable because of the weakness of the lines. The ratio of each segment's DEM with the mean spectrum DEM (*lower panels*) show that the plasma distribution in temperature is essentially the same in all segments except 1(0) and 2(1). These latter show the largest downflow velocities (see Fig. 5).

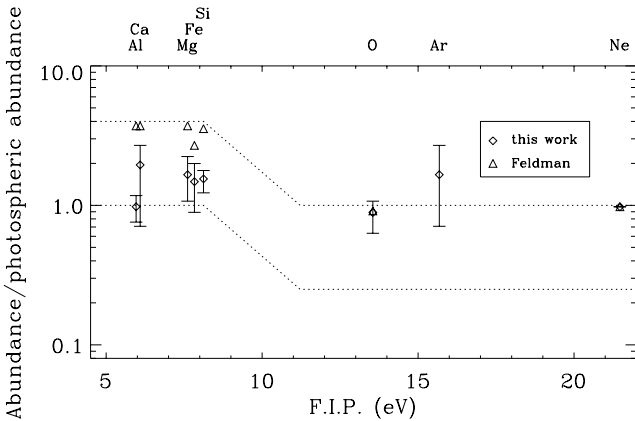


**Fig. 7.** Derived elemental abundances for our CDS s6011r00 observation compared with the Feldman et al. (1992) coronal abundances. Abundances are plotted as ratios with the photospheric values taken from Feldman (1992). The  $3\text{-}\sigma$  confidence interval is also reported, obtained for all elements except Mg by a Monte Carlo simulation. The  $3\text{-}\sigma$  confidence interval for Mg is obtained by propagation of errors via the Mg/Ne constraint (see text). Ne is taken as reference.

the atomic data and then evaluated the elemental abundances by a  $\chi^2$  minimization for a given DEM. The DEM has therefore been re-evaluated with the new abundances and the procedure iterated until the maximum correction to the abundances was below 10%. This procedure allows a good determination of the abundance ratios of elements whose lines form at close temperatures. In such cases, the uncertainties in the DEM reconstruction tend to cancel out and the dominant uncertainties on the abundance ratios derive from the atomic data and observational uncertainties.

In the DEM analysis carried out here, however, the low temperature range ( $5.0 \leq \log T_e \leq 5.8$ ) is sampled by high FIP elements and the high temperature range ( $5.8 < \log T_e \leq 6.0$ ) by low FIP elements. As a consequence, above  $\log T_e = 5.8$  variations of abundances of the low FIP elements cannot be effectively disentangled from variations of the DEM with temperature, although the relative abundances amongst low FIP elements remains well constrained.

In order to overcome such difficulties, we have used an additional constraint based on the Mg VI (349.2 Å)/Ne VI (562.8 Å) line intensity ratio. The peaks of temperature of formation for Mg VI and Ne VI are essentially the same, and this attractive characteristic has been widely used in deriving coronal Mg/Ne abundances (e.g., Widing & Feldman 2001, and references therein), often with Ne used as a proxy for the high FIP group of elements and Mg for the low FIP group of elements. The Mg VI (349.2 Å)/Ne VI (562.8 Å) line intensity ratio observed by CDS-NIS has been used, for instance, by Young & Mason (1997) to derive Mg/Ne abundance variations in a recently emerged flux region.

Note that neither Mg VI (349.2 Å) nor Ne VI (562.8 Å) are reproduced satisfactorily by the DEM analysis (see Sects. 4.2.5 and 4.2.3), the most likely cause being inaccuracies in the atomic modelling. Lacking other trustworthy constraints, however, we impose the criterion that the solution reproduces the observed Mg VI (349.2 Å)/Ne VI (562.8 Å) line intensity ratio within 10%.

The results for the mean spectrum are shown in Fig. 7 together with the Feldman et al. (1992) coronal abundances for comparison. In Fig. 7, abundances are shown as ratios to their photospheric values (taken from Feldman 1992). The  $3\text{-}\sigma$

**Table 6.** Abundance enhancement factors (with respect to photospheric composition) for the low FIP elements in the selected segments.  $\beta$  is the FIP bias deduced from the observed Mg VI (349.2 Å)/Ne VI (562.8 Å) line intensity ratio as in Young & Mason (1997). The result for Ar in segment 2(1) is not reported because the estimated error is very large.

Region	Segment	Enhancement factor							$\beta$
		Al	Ca	Mg	Fe	Si	O	Ar	
Extended brightening	1(0)	$0.5^{+0.2}_{-0.2}$	$1.9^{+0.9}_{-1.5}$	$1.7^{+0.3}_{-0.3}$	$1.2^{+0.6}_{-0.5}$	$1.5^{+0.2}_{-0.3}$	$0.6^{+0.2}_{-0.2}$	$2.1^{+0.9}_{-0.9}$	3.6
	2(1)	$1.1^{+0.6}_{-0.5}$	$1.7^{+1.9}_{-1.0}$	$1.9^{+0.3}_{-0.3}$	$2.2^{+0.7}_{-0.7}$	$2.3^{+0.5}_{-0.5}$	$0.6^{+0.2}_{-0.1}$		3.5
Narrow brightening	3(4)	$1.1^{+0.4}_{-0.4}$	$1.7^{+1.5}_{-1.1}$	$1.7^{+0.3}_{-0.3}$	$2.0^{+0.8}_{-0.6}$	$1.7^{+0.4}_{-0.5}$	$0.9^{+0.2}_{-0.1}$	$1.8^{+1.2}_{-0.8}$	3.5
	5(7U)	$1.0^{+0.5}_{-0.4}$	$3.7^{+1.9}_{-1.1}$	$1.5^{+0.3}_{-0.3}$	$0.9^{+0.3}_{-0.3}$	$1.0^{+0.2}_{-0.2}$	$0.9^{+0.2}_{-0.1}$	$1.5^{+1.0}_{-0.7}$	3.2
	7(8U)	$0.8^{+0.4}_{-0.5}$	$4.8^{+2.8}_{-1.8}$	$1.7^{+0.3}_{-0.3}$	$1.4^{+0.5}_{-0.3}$	$1.6^{+0.4}_{-0.3}$	$1.0^{+0.2}_{-0.2}$	$0.5^{+0.6}_{-0.3}$	3.2
	8(9)	$0.9^{+0.5}_{-0.6}$	$2.1^{+0.9}_{-0.6}$	$1.7^{+0.3}_{-0.3}$	$0.7^{+0.3}_{-0.2}$	$1.2^{+0.2}_{-0.3}$	$1.0^{+0.2}_{-0.2}$	$1.3^{+0.8}_{-0.6}$	3.1
Dark regions	4(7L)	$1.1^{+0.8}_{-0.8}$	$2.6^{+1.4}_{-1.0}$	$0.8^{+0.3}_{-0.3}$	$0.9^{+0.4}_{-0.4}$	$1.3^{+0.3}_{-0.3}$	$0.7^{+0.2}_{-0.1}$	$2.3^{+0.8}_{-1.3}$	1.5
	6(8L)	$0.6^{+0.4}_{-0.5}$	$2.3^{+1.4}_{-1.7}$	$1.2^{+0.3}_{-0.3}$	$0.6^{+0.2}_{-0.2}$	$1.1^{+0.2}_{-0.2}$	$0.9^{+0.2}_{-0.2}$	$2.1^{+1.2}_{-1.7}$	2.6

confidence interval is also reported, obtained for all elements except Mg by a Monte Carlo simulation. The  $3\text{-}\sigma$  confidence interval for Mg is obtained by propagation of errors via the Mg/Ne constraint discussed above. We remind the reader that Ne is taken as reference.

In the mean spectrum all elements are found close to photospheric composition, with enhancement factors below two except for Ca whose abundance is 2.1 photospheric. The results for Al and Ca, however, must be considered with caution. In fact, using lines of Al X and Ca X only, for instance, the derived abundance for Al and Ca would be about four times photospheric, and therefore close to coronal values. Including all lines listed in Table 1 we derive abundances close to photospheric for Al and Ca too. A likely explanation for this situation is that the accuracy of the atomic data for some of the ions of Al and Ca are still below the requirements for this type of analysis. An alternative explanation is that there is some enrichment process taking place, which affects some of the ionisation stages of the elements with lowest FIP more than others. The derived abundance for the high FIP element Ar is consistent with photospheric composition; the large error bar is due to the fact that only one Ar line can be used for the analysis. The abundance of O is everywhere very close to photospheric composition (except in segment 1(0) for which our analysis is uncertain) with a  $3\text{-}\sigma$  uncertainty of typically 20%.

The same procedure has been applied to the spectra from the selected segments (Table 6). We find that the abundance of all elements remains essentially photospheric, except that of Ca, as discussed above for the mean spectrum. As in the mean spectrum, the abundance of Ar has large error bars, especially in segment 2(1).

Following Widing & Feldman (2001) we indicate with  $\beta$  the FIP bias based on the Mg/Ne abundance ratio relative to the photospheric composition (i.e.  $\beta = 1$  indicates photospheric composition). We derive  $\beta$  from the observed Mg VI (349.2 Å)/Ne VI (562.8 Å) line intensity ratio as in Young & Mason (1997). Table 6 indicates that  $\beta \approx 3$  in all segments (as well as in the mean spectrum) except in the dark Mg IX regions, where  $\beta$  is closer to unity. This comparison,

**Table 7.** Comparison of the median  $I_{\text{th}}/I_{\text{obs}}$  between NIS-1 and NIS-2 lines for the ions O III, Ne IV, and Ne V.

Ion	MEDIAN $I_{\text{th}}/I_{\text{obs}}$	
	NIS-1	NIS-2
O III	0.2	0.9
Ne IV	0.6	1.2
Ne V	0.9	1.6

on the one hand, confirms that the Mg abundance is essentially constant from segment to segment; on the other hand, it shows that the Mg/Ne abundance ratio inferred from the observed Mg VI (349.2 Å)/Ne VI (562.8 Å) line intensity ratio differs from the DEM results by a factor of 2. This is due to the underlying assumption of a constant DEM in the line ratio technique combined with the temperature (and density) dependence of the Mg VI (349.2 Å)/Ne VI (562.8 Å) line intensity ratio. An assessment of the accuracy of the atomic population modelling for Mg VI and Ne VI is, however, required to make a sound comparison between the two techniques.

#### 4.5. NIS-1/NIS-2 cross-calibration uncertainties

Landi et al. (1997), considering ions whose lines are observed in both NIS channels, found discrepancies that they attributed to errors in the NIS-1/NIS-2 cross-calibration. They derived a relative calibration from in-flight data and this together with the preliminary results from the laboratory calibration provided a basis for version 1 of the CDS NIS intensity calibration. As detailed in Lang et al. (2002), the calibration has been revised since then and the burn-in corrections, particularly with the adoption of the wide-slit burn-in correction, are now improved. Thus without repeating their work with the present day data reduction and calibration software it is very difficult to make any comparisons. However, the revisions to the calibration since their work have substantially reduced the discrepancies. In our analysis, lines of O III, Ne IV, and Ne V show a mismatch between NIS-1 and NIS-2 too. In fact, for such ions, it looks like

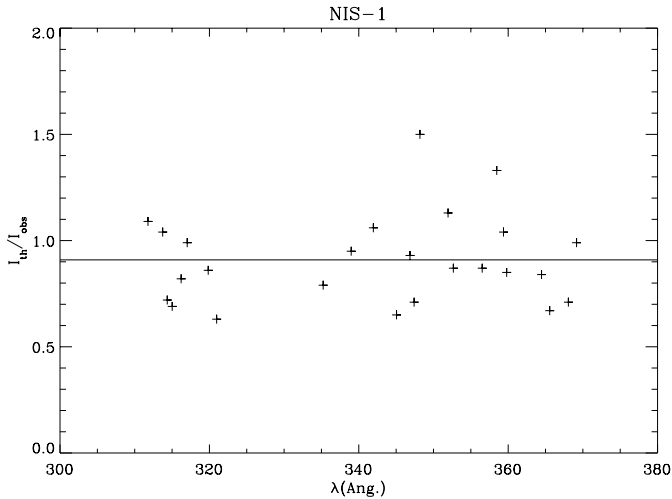


**Fig. 8.**  $I_{\text{th}}/I_{\text{obs}}$  ratio for NIS-1 lines with  $(\sigma_0\chi_i)^2 \leq 3$ , excluding also lines affected by unknown blends or large uncertainties in the atomic data (crosses), together with a  $I_{\text{th}}/I_{\text{obs}} = \text{const.}$  least-square fit.

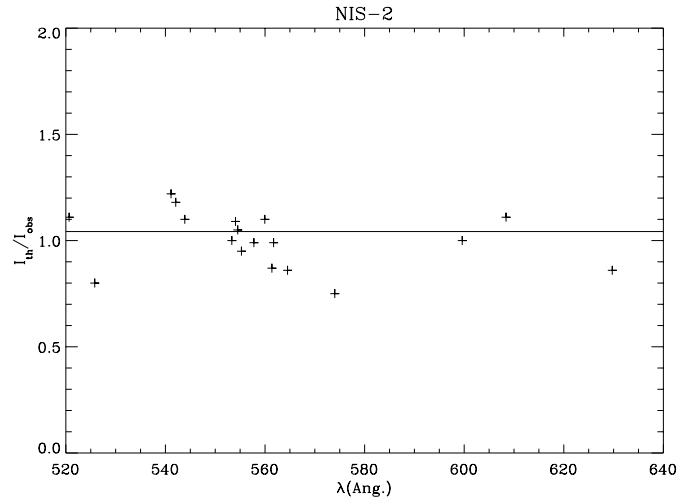


**Fig. 9.** Same as Fig. 8 for NIS-2 lines. From the comparison with the previous plot we infer that the error in the NIS-1/NIS-2 cross calibration is at most 10%.

either NIS-1 lines are underestimated or NIS-2 lines are overestimated (or both) by the DEM reconstruction (see Sects. 4.2.3, 4.2.4, and 4.2.5). Similarly to the Landi et al. (1997) analysis, the correction factor implied by such lines is rather large, being between a factor 2 and 4, and greater than the uncertainties assigned to the intensity calibration<sup>1</sup>.

We have therefore performed some numerical experiments in which the responsivity of one of the two channels has been multiplied by an arbitrary correction factor to take into account possible errors in the NIS-1/NIS-2 cross-calibration. We found that a correction of the NIS-1/NIS-2 relative calibration greater than approximately 20% increases the reconstruction errors for the lines used in the integral inversion (labelled “i” in Tables 1 and 5) and for those chosen for the comparison in the forward sense (labelled “f” in Tables 1 and 5) well above the observational uncertainties. Such a correction would therefore produce inconsistencies amongst those lines which have been selected in both channels because of their reliability. Note that, although the  $G$ -functions of these lines peak at different temperatures<sup>2</sup>, such inconsistencies show up because the overlapping part of the  $G$ -functions still constrains the DEM substantially. In the *data adaptive smoothing approach* used here (see Paper I for a description) the automatic smoothing tends to adjust the  $\lambda$ -parameter in response to the change in the relative calibration to fit both NIS-1 and NIS-2 lines in the list used for the integral inversion, still maintaining the smoothness of the DEM. In the present case, where lines from both channels are mixed in the list, if we introduce an increasing correction factor in the NIS-1/NIS-2 relative calibration, we have first a distortion of the DEM with the theoretical intensities increasingly failing to reproduce the observations, then either the automatic smoothing fails or the solution becomes unacceptable. Using an arbitrary smoothing method, it would still be possible to

reproduce the intensities with an oscillatory DEM with multiple peaks, like that computed by Landi & Landini (1997), but such a solution is not justified by the information content of the data.

In Figs. 8 and 9 we plot the  $I_{\text{th}}/I_{\text{obs}}$  ratio for lines with  $(\sigma_0\chi_i)^2 \leq 3$  (excluding also lines affected by unknown blends or large uncertainties in the atomic data), together with a  $I_{\text{th}}/I_{\text{obs}} = \text{const.}$  least-square fit on both NIS-1 and NIS-2 data. Comparing the two fits, we infer that the uncertainty in the cross-calibration is at most 10%. This should be considered only an upper limit, given the high rejection value adopted for  $(\sigma_0\chi_i)^2$ .

We therefore conclude that the discrepancies seen in O III, Ne IV, and Ne V cannot be ascribed to errors in the cross-calibration of the NIS channels.

## 5. Conclusions

This work builds on the spectral analysis of Brooks et al. (1999), exploiting the DEM in the spectral analysis of a quiet Sun area observed by SOHO-CDS and addressing the issue of how the DEM of small subareas (indicated here as segments of the whole raster sequence) combine to give the DEM of a larger area. The DEM analysis is also exploited to improve the line identification performed by Brooks et al. (1999) and to investigate possible elemental abundance variations from region to region.

The distribution of the plasma in temperature is found to be essentially the same in all segments except those around the extended Mg IX brightening (1(0) and 2(1)). These latter are the regions with the lowest electron density and *downflow* velocities of the order of  $50 \text{ km s}^{-1}$  (Fig. 5), which are expected to contain plasma not in ionisation equilibrium. This situation is interpreted here as indicating that, in regions where  $\log N_e > 7.3$  and downflow velocities are less than  $50 \text{ km s}^{-1}$ , radiative cooling and (or) conductive terms dominate(s) the energy balance in the QS upper transition region and inner corona. In such conditions the DEM differs only by a roughly

<sup>1</sup> Version 4 of the CDS calibration is used in the present analysis, along with the data reduction as detailed in Lang et al. (2000).

<sup>2</sup> To improve the conditioning of the problem, the use of lines with similar  $G$ -functions in the integral inversion is avoided.

constant factor depending on the total amount of heating in that region. The segments around the extended Mg IX brightening might correspond to a combination of the tops of large loops whose footpoints lie outside the selected segments and of compact loops which do not reach coronal temperature and are thermally decoupled from the plasma emitting in Mg IX. Such compact loops are known to show high velocities (see, e.g., Lanzafame et al. 1999). The analysis carried out in this work shows that complex structure in the DEM due to inhomogeneities, such as multiple peaks, is not justified by the data and is not expected unless uncertainties affect large areas of the region analysed.

The elemental abundances are found to be close to photospheric composition and do not show significant variations from region to region. Only the Ca abundance seems to be enhanced with respect to photospheric values with some variation from region to region, but the results are quite uncertain since the scatter of spectral lines of the Ca ions is rather large. The Al abundance is also rather uncertain for the same reasons. Note that the use of Al X and Ca X only would lead to estimated abundances about four times photospheric in the mean spectrum, and a photospheric composition is inferred only using all lines listed in Table 1.

Two indications of departures from ionisation equilibrium are found. The first is that when  $\log N_e < 7.3$  and the velocity exceeds  $50 \text{ km s}^{-1}$  the DEM reconstruction has higher uncertainties. In such conditions the plasma can travel a hydrostatic scale-height in 300 s at  $\log T = 5.5$ , which is an order of magnitude shorter than the relaxation time-scales for the ground states at the inferred electron densities. This affects the calculation of the DEM over an area of approximately 2 by 80 arcsecs<sup>2</sup>, but the effect is less important on the calculation of the DEM based on the spectrum averaged over 20 by 240 arcsecs<sup>2</sup>. The second indication comes from the comparison between the Li-like Mg X (624.95 Å) and the Be-like Mg IX (368.057 Å) in each segments, which points to an overabundance of the Li-like stage (longer relaxation time-scale for the ground state) with respect to equilibrium conditions. This is supported also by the comparison between the Li-like Al XI (550.04 Å) and the Be-like Al X (332.788 Å), which show the same systematic behaviour as the Mg X and Mg IX lines. A viable alternative explanation of this latter behaviour is, however, that recombination to the excited term  $2s 2p^1P$  of the Be-like ions or ionisation to it from e.g. the  $2s 2p^2 4P$  term in the B-like ions give a contribution which is not accounted for in our analysis since level-resolved ionisation balance calculations for Mg and Al are not yet available.

We note that the relaxation time-scales for ground levels presented in Paper I are evaluated directly from the ionisation/recombination cross-sections. The time required to reach the ionisation equilibrium can be much shorter than these values if departures are small. Hydrodynamic calculations (see, e.g., Spadaro et al. 2003; Lanza et al. 2001) indicate that such departures for a single loop may last only for short times and may be not too large. The analysis presented here indicates that departures from ionisation equilibrium may significantly affect the analysis on small areas (of the order of 2 by 80 arcsec<sup>2</sup> in the present observations), but when considering an

average on larger areas (of the order of 20 by 240 arcsec<sup>2</sup> in the present observations) they tend to be of less importance because most of the plasma appears to be close to ionisation equilibrium. Departures from ionisation equilibrium, therefore, may not invalidate the DEM analysis on large areas, allowing us to derive a distribution in temperature for the bulk plasma in quasi-equilibrium. For such areas the DEM still represents a useful support for the spectral analysis, but accurate results could not always be obtained because of the presence of relatively small transients of short duration.

Significant discrepancies are generally found for density sensitive lines. Some multiplet that were reproduced within the observational uncertainties in the SERTS-89 active region analysis (Paper I) are not reproduced accurately in the present analysis because they have larger density sensitivity in the range of electron densities involved here. This is likely to be caused by the assumption of uniform electron density (or uniform electron pressure) and a bivariate DEM (differential in temperature and density) approach would be required.

Accurate results are also prevented by the uncertainties in the atomic modelling of some ions, which confuses the picture further. Because of this, we are sometimes unable to find with confidence the cause of the observed discrepancies. Unfortunately, such uncertainties would prevent also a reliable bivariate DEM approach, and therefore the possibility of taking into account unresolved inhomogeneities of the observed plasma. In some instances, e.g. O IV, Ne VI, Mg VI, Si X, and Mg VII, our analysis reveals unambiguously errors in the atomic data.

*Acknowledgements.* CDS was built and is operated by a consortium led by the Rutherford Appleton Laboratory and which includes the Mullard Space Science Laboratory, the NASA Goddard Space Flight Center, Oslo University and the Max-Planck-Institute for Extraterrestrial Physics, Garching. SOHO is a mission of international cooperation between ESA and NASA. This work was done in the context of the ADAS project. The authors thank an anonymous referee for useful comments on the original manuscript.

## References

- Brooks, D. H., Fischbacher, G. A., Fludra, A., et al. 1999, *A&A*, 347, 277
- Dere, K. P., Landi, E., Mason, H. E., Monsignori Fossi, B. C., & Young, P. R. 1997, *A&AS*, 125, 149
- Edlén, B. 1983a, *Phys. Scripta*, 28, 51
- Edlén, B. 1983b, *Phys. Scripta*, 28, 48
- Edlén, B. 1984, *Phys. Scripta*, 30, 135
- Edlén, B. 1985a, *Phys. Scripta*, 31, 345
- Edlén, B. 1985b, *Phys. Scripta*, 32, 59
- Edlén, B. 1985c, *Phys. Scripta*, 32, 86
- Fawcett, B. C. 1975, *Atomic Data and Nuclear Data Tables*, 16, 138
- Feldman, U. 1992, *Phys. Scripta*, 46, 202
- Feldman, U., Mandelbaum, P., Seely, J. F., Doschek, G. A., & Gursky, H. 1992, *ApJS*, 81, 387
- Harrison, R. A. 1997, *Sol. Phys.*, 175, 467
- Harrison, R. A., Sawyer, E. C., Carter, M. K., et al. 1995, *Sol. Phys.*, 162, 233
- Harrison, R. A., Lang, J., Brooks, D. H., & Innes, D. E. 1999, *A&A*, 351, 1115
- Harrison, R. A., Harra, L. K., Brkovic, A., & Parnell, C. E. 2003, *A&A*, 409, 755

- Innes, D. E., Inhester, B., Axford, W. I., & Wilhelm, K. 1997, *Nature*, 386, 811
- Jupén, C., Isler, R. C., & Träbert, E. 1993, *MNRAS*, 264, 627
- Kelly, R. L. 1987, *J. Phys. Chem. Ref. Data*, 16, Supp. 1
- Landi, E., & Bhatia, A. K. 2003, *ApJ*, 589, 1075
- Landi, E., & Landini, M. 1997, *A&A*, 327, 1230
- Landi, E., Landini, M., Pike, C. D., & Mason, H. E. 1997, *Sol. Phys.*, 175, 553
- Landi, E., Storey, P. J., & Zeippen, C. J. 2004, *ApJ*, 607, 640
- Lang, J., Kent, B. J., Breeveld, A. A., et al. 2000, *J. Opt. A*, 2, 88
- Lang, J., Brooks, D. H., O'Mullane, M. G., et al. 2001, *Sol. Phys.*, 201, 37
- Lang, J., Thompson, W. T., Pike, C. D., Kent, B. J., & Foley, C. R. 2002, in *The Radiometric Calibration of SOHO. ISSI Scientific Report SR-002*, ed. A. Pauluhn, M. C. E. Huber, & R. von Steiger, 105
- Lanza, A. F., Spadaro, D., Lanzafame, A. C., et al. 2001, *ApJ*, 547, 1116
- Lanzafame, A. C., Spadaro, D., Consoli, L., Marsch, E., & Brooks, D. H. 1999, in *The 8th SOHO workshop: Plasma Dynamics and Diagnostics in the Solar Transition Region and Corona*, ed. J.-C. Vial, & Kaldeich-Schürman, 429
- Lanzafame, A. C., Brooks, D. H., Lang, J., et al. 2002, *A&A*, 384, 242
- Martin, W. C., Sugar, J., Musgrove, A., & Dalton, G. R. 1995, *NIST Database for Atomic Spectroscopy, Version 1.0, NIST Standard Reference Data base 61*
- McWhirter, R. W. P., & Summers, H. P. 1984, in *Applied Atomic Collision Physics* ed. C. F. Barnett, & M. F. A. Harrison (Academic Press), 2, 51
- Moore, C. E. 1993, in *Tables of Spectra of Hydrogen, Carbon, Nitrogen and Oxygen Atoms and Ions*, ed. J. W. Gallacher, CRC Series in Evaluated Data in Atomic Physics (CRC Press)
- Shirai, T., Funataka, Y., Mori, K., et al. 1990, *J. Chem. Phys. Ref. Data*, 19, 127
- Spadaro, D., Lanza, A. F., Lanzafame, A. C., et al. 2003, *ApJ*, 582, 486
- Summers, H. P. 1994, *ADAS manual, JET Joint Undertaking, JET-IR(94)07*
- Summers, H. P. 2001, *The ADAS manual, version 2–3*, <http://adas.phys.strath.ac.uk>
- Thomas, R. J., & Neupert, W. M. 1994, *ApJS*, 91, 461
- Thompson, A. M. 1990, *A&A*, 240, 209
- Thompson, A. M. 1991, in *Intensity Integral Inversion Techniques: a Study in Preparation for the SOHO Mission*, ed. R. A. Harrison, & A. M. Thompson, RAL Report No. RAL91-092
- Widing, K. G., & Feldman, U. 2001, *ApJ*, 555, 426
- Wiese, W. L., ed. 1985, *Spectroscopic Data for Iron*, ORNL No. 6089/V4 (Oak Ridge National Laboratory)
- Young, P. R., & Mason, H. E. 1997, *Sol. Phys.*, 175, 523
- Young, P. R., Landi, E., & Thomas, R. J. 1998, *A&A*, 329, 291
- Young, P. R., Del Zanna, G., Landi, E., et al. 2003, *ApJS*, 144, 135